

Optical investigation of large-scale boundary-layer structures

Matthew R. Kemnetz* and Stanislav Gordeyev †

University of Notre Dame, Notre Dame, Indiana, 46446, USA

An investigation of large-scale boundary-layer structures using optical wavefront sensing techniques is described. Measurements were conducted in Notre Dame’s Tri-Sonic facility at $M = 0.4$ and 0.5 with a range of sampling frequencies and spatial resolutions as well as the Merrill Wind Tunnel facility at Caltech at $M = 0.03$. In this paper we present several techniques for determining optical wavefront energy spectra and the implications of those techniques to large-scale structures. Finally we investigate the effect of Reynolds number on the wavefront spectra in a turbulent boundary-layer. The data has shown an increase in Reynolds number causes a significant energy shift toward lower St_δ , indicating that optically active large scale structures grow larger with increase in Reynolds number.

Nomenclature

λ	Wavelength
ρ	fluid density
$\hat{\theta}$	Deflection angle spectra
σ_f	Standard deviation of f
σ_g	Standard deviation of g
\bar{f}	Average of f
\bar{g}	Average of g
$f(x, y)$	Current wavefront
$g(x, y)$	Next wavefront
C	Cross correlation between f and g
OPD	Optical Path Difference
OPL	Optical Path Length
TTP	Tip Tilt Piston
$SHWFS$	Shack-Hartmann Wavefront Sensor
\hat{W}	Wavefront energy spectra

I. Introduction

LARGE-SCALE structures present in turbulent boundary layers have long been of interest to researchers. Large-scale structures, located in the outer part of the subsonic boundary layer (BL) carry an important role in boundary-layer dynamics. They are responsible for entrainment processes and, via a link with small-scale structures near the wall, instantaneous drag near the wall.¹ While there exists a large body of experimental research concerning large-scale structures,² there remain open questions about their topology, dynamics, and their interaction with near-wall structures. Until recently, the experimental study of such topics has been difficult and limited.³ Although the precise physical mechanism for such large-scale motions is still hotly debated, they are likely caused by organized packets of hairpin vortices traveling at the same

*Graduate Student, Department of Aerospace and Mechanical Engineering, Hessert Laboratory for Aerospace Research, Notre Dame, IN, 46556, AIAA Student Member.

†Research Associate Professor, Department of Aerospace and Mechanical Engineering, Hessert Laboratory for Aerospace Research, Notre Dame, IN, 46556, AIAA Associate Fellow.

convective speed.^{4,5} Experimental work by Adrian et al.⁶ demonstrated in the outer layer, hairpin vortices align themselves in the streamwise direction creating long meandering regions of velocity deficit.⁶

Large-scale structures are often difficult to investigate experimentally partially due to the trade-off between spatial resolution and region of interest. Fine spatial resolution inhibits the ability to capture the larger picture necessary to study large-scale structures. Traditionally, large-scale structures are characterized by the velocity field which is measured using hot-wires or a PIV technique. These techniques give either detailed temporal information in small spatial domain (hot-wires) or potentially time-resolved spatial velocity field information in a plane (PIV). An alternative way to non-intrusively study the characteristics of large-scale structures in boundary layers is to measure related density distortions. Turbulent density fluctuations that are present in the region immediately around an aerodynamic vehicle alter the local speed of light passing into and/or out of the aircraft through the turbulent region. This phenomenon is known as the aero-optic problem.^{7,8} As planar wavefronts propagate through these unsteady density distributions, they get distorted and these distortions can be accurately measured by various wavefront sensors. One very useful feature of these measurements is that they are non-intrusive by nature and can be easily applied at high speeds,^{9,10} including hypersonic ones.¹¹

In Dennis et al.³ the researchers coupled high speed PIV measurements with Taylors Frozen Flow Hypothesis to construct quasi-instantaneous velocity fields. It was previously demonstrated by the same researchers that when considering large scale structures, Taylors hypothesis is a valid approximation.¹² In this work, we look to investigate large-scale turbulent structures by measuring aero-optical distortions using a wavefront sensor and applying a similar approach to Dennis et al. Here we couple Taylors Hypothesis with optical wavefront measurements, trading time for space, to capture a better understanding of large-scale optical structures within a turbulent boundary layer. It is important to note that optical structures are closely related to physical turbulent structures but they are distinct. The optical quantity measured (OPD) is an integrated quantity; nonetheless, recent simultaneous PIV/Optical measurements¹³ demonstrated that optical measurements provided valuable insight into the investigation of large scale turbulent boundary layer structures.

The main focus of this paper is the analysis of optical wavefront energy spectra. In this work we investigate different derivations of wavefront energy spectra from deflection angle spectra, the direct computation of wavefront energy spectra from optical wavefronts, and finally the computation of wavefront energy spectra using the quasi-instantaneous adaptation of Taylors Frozen Flow Hypothesis. Each technique has its own benefits and drawbacks and these will be discussed accordingly.

II. Experimental Measurements

Wavefront data used in this work were collected in two different facilities. Low-speed experiments were conducted in the Merrill Wind Tunnel facility at Caltech (later called Caltech experiment) under the following flow conditions: $Re_\theta = 2100$, $Re_\tau = 1200$, $M_\infty = 0.03$, $\delta = 35$ mm. The wall of the boundary layer plate was heated to $20^\circ C$ above the free stream temperature. The schematic of the set-up can be seen in Figure [1(a)]. Cress¹⁴ and Gordeyev et al¹⁵ showed that if the boundary layer wall is moderately-heated relative to the free stream density, it will not modify the underlying velocity structure. Instead, moderate heating will simply introduce passive temperature markers in the boundary layer and effectively amplify aero-optical levels. By introducing moderate-temperature mismatch between the wall and the boundary layer, it is possible to thermally tag and investigate three-dimensional large-scale structures in incompressible boundary layers using optical methods.¹³

Wavefronts through the boundary layer in the wall-normal direction were collected with a Shack-Hartmann wavefront with a 50 mm-diameter. 20,000 wavefronts with 40x40 resolution were collected using a sampling frequency of 1,500 Hz.

High-speed experiments were conducted in the Hessert Tri-Sonic Wind Tunnel (TWT) at the University of Notre Dame (later called Notre Dame experiment). The TWT is a continuous flow in draft wind tunnel with an inlet contraction ratio of 150:1, and a cross-section of 10 cm \times 9.9 cm. The tunnel test section is constructed of Plexiglas. The test section was 160 cm in length from the end of the inlet to the diffuser with optical windows installed on the upper and lower walls from 130 cm to 150 cm. Free stream velocity was measured using a static pressure port just upstream of the optical window and was held constant at $M = 0.4$ for the duration of the measurements. The boundary layer thickness, δ , at the measurements location was found to be approximately 15.6 mm, with δ^* to be 2.4 mm and $\theta = 1.74$ mm. Based on these values, $Re_\tau =$

4,780 and $Re_\theta = 15,500$. For these experiments the laser beam was going through both optically-aberrating boundary layers on the opposite tunnel walls, see Figure [1(b)].

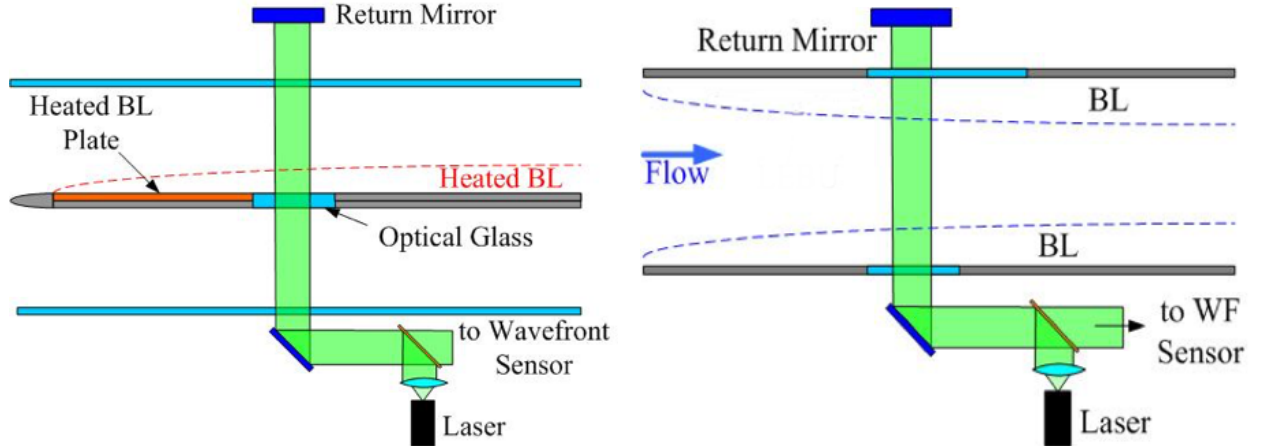


Figure 1. Schematic of Wavefront measurements using Shack-Hartmann 2-D wavefront sensor at Caltech 1(a) and Notre Dame 1(b).

Similar to the Caltech experiments, full circular 2-D wavefronts, resolved in both the streamwise (x) and the spanwise (z) directions, were collected using a high-speed Shack-Hartmann Wavefront Sensor (SHWFS).

Name	M	Subapertures	Ap/δ	Sampling Frequency (Hz)
F04	0.5	46x46	3.88	49,000
F06	0.5	25x34	2.84	100,000
F12	0.5	21x22	3.02	130,000
C01	0.03	40x41	1.37	25,000

Table 1. Experiment Matrix

The number of subapertures and the sampling frequency for each test case can be seen in the Table [1]. Time series of spatially-resolved wavefronts were calculated from Shack-Hartmann images using in-house developed software.

III. Results

There are several different ways of computing wavefront streamwise spectra. Below we will discuss some of them.

A. Wavefront Spectrum from Deflection Angle Spectrum

The Shack-Hartmann sensor measures the temporal evolution of the gradient of the wavefront. This quantity is also called local deflection angle,

$$(\theta_x, \theta_y) = -\nabla W.$$

Malley et al.¹⁶ proposed to compute streamwise slices of a wavefront by using the streamwise component of the deflection angle and utilize the fact that the aero-optical distortions convect with the flow. In this case, the streamwise gradient of the wavefront can be replaced by its temporal derivative and the wavefront can be computed by integrating the time series of the deflection angle,¹⁷

$$\theta_x = -\frac{dW}{dx} = -\frac{1}{U_c} \frac{dW}{dt}.$$

The convective speed can be measured by cross-correlating deflection angle measurements at two or more locations separated in the streamwise direction, the so-called Malley probe.¹⁷ This method typically uses only a few spatial points, so wavefront measurements can be made at very high frequency.

Deflection angle spectra can be seen in Figure [2(a)]. As expected the peak location for all cases occurs around $St_\delta = 1$. But, there are some significant deviations on both the low end of the spectrum, and the high end.

Deflection angle spectra, $\hat{\theta}$, is related to wavefront spectra, \hat{W} , by Eq. [1]

$$\hat{W}(f) = U_c \frac{\hat{\theta}(f)}{2\pi i f} \quad (1)$$

For the purposes of this paper the generation of optical wavefront energy spectra developed using Eq. [1] will be denoted as Method (A). It is important to recognize that Method (A) completely ignores the spanwise component of the deflection angle in order to compute the streamwise wavefront spectrum. Wavefront Energy spectra computed from deflection angle data can be seen in Figures[2(b)] and [2(c)].

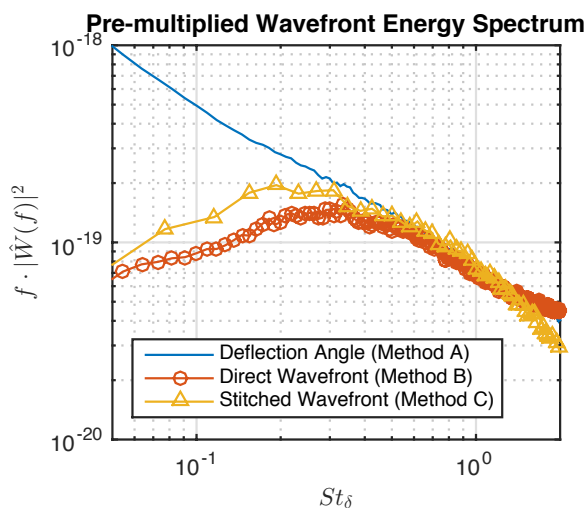
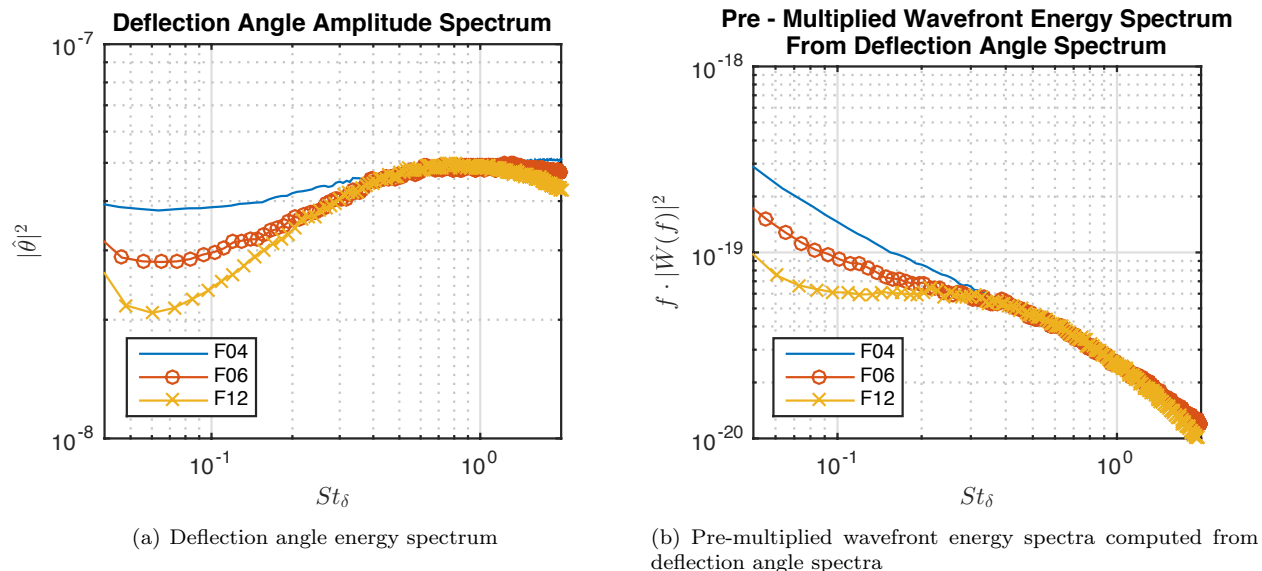


Figure 2.

B. Direct Wavefront Energy Spectra

Another way to compute a wavefront is to use both components of the deflection angle and to reconstruct two-dimensional wavefront sequences using the Southwell method.¹⁸ From time-series of wavefronts, the wavefront power spectrum can be computed. This direct computation of wavefront spectra will be denoted as Method (B).

However, the method has its own drawbacks. Firstly, wavefronts at a given time are known up to a constant, called a piston mode. Second, mechanical vibrations of the tunnel and optical set-up add unphysical jitter to the tip/tilt component of the wavefronts. Therefore, in the analysis of the wavefront data tip, tilt, and piston are always removed from the apertured wavefronts. Is it straightforward to show¹⁹ that removing these components is equivalent of applying a high-pass filter to the wavefront data; this filter depends on the aperture size, the so-called aperture-effects.^{17,18} The high-pass nature of the filter means that a portion of the wavefront spectrum at low frequency, related to the large-scale structure, might be modified and some of the information pertaining to large-scale coherent structures is lost.

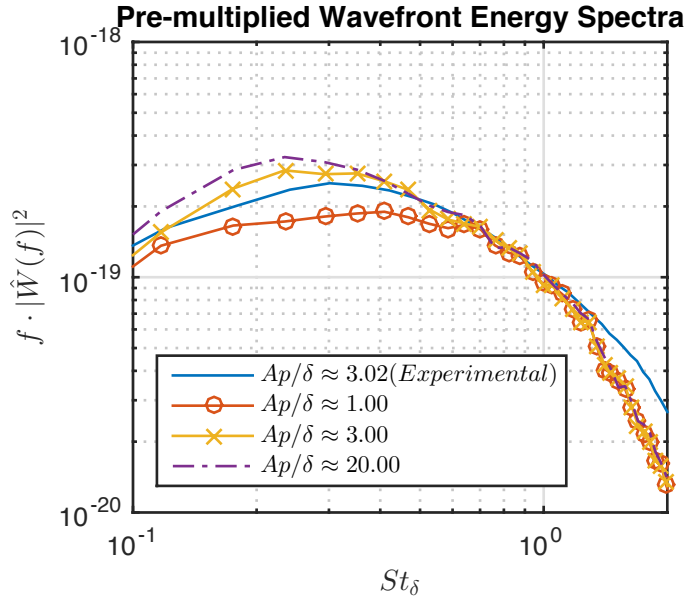


Figure 3. Aperture effects of direct wavefront energy spectra (Method (B))

Premultiplied wavefront energy spectra computed using Methods (A) and (B) can be seen in Figure [2(c)]. Notice that while properly resolving the high end of the frequency range, Method (A) actually produces a diverging spectrum at low frequencies, compared to Method (B), where there is no divergence in the energy for large scale structures. This divergence at low frequencies for Method (A) is obviously non-physical and is caused by ignoring spanwise correlations in the wavefront. Therefore, computing wavefront energy spectra using Method (A) is not particularly ideal for studying large-scale boundary layer structures.

Figure [3] demonstrates the affect of the aperture size in the pre-multiplied wavefront spectrum, using Method (B). The data in Figure [3] was produced both experimentally and through the “Stitching Method” discussed in detail later in the paper. The Stitching Method was used to produce time-series of optical wavefronts with varying effective aperture sizes. Notice the increase in energy toward lower frequencies as well as the shift in peak location as the aperture size increases. There is very close agreement in peak location between $Ap/\delta \approx 3.00$ and $Ap/\delta \approx 20.00$. This means for experimental purposes an aperture of around $Ap/\delta \approx 3 - 5$ should adequately capture the peak location in the power spectra and therefore is sufficient to characterize large scale structures.

The energy deficit and shift in peak location seen between the $Ap/\delta \approx 1.00$ and $Ap/\delta \approx 3.00$ cases can be attributed to tip/tilt/piston removal. To generate the time series data used in Figure [3] a very long (approximately 300δ) wavefront was stitched together using the algorithm presented in this paper. Space was then traded for time using a constant convective speed and fixed sampling frequency. In this manner wavefront time series of arbitrary Ap/δ could be generated from stitched wavefront data. This process can

be thought of as the inverse of the stitching algorithm presented in this paper. In Figure [3] a constant convective speed was used and it will be shown later that the convective speed is indeed not constant. This might describe the slight discrepancy between the directly computed $Ap/\delta \approx 3.02$ case and the $Ap/\delta \approx 3.00$ case which was generated from stitched wavefront data.

C. Wavefront Reconstruction Using “Stitching” Method

As it was shown before, using the streamwise deflection angle component, Method (A), gives unphysical results at low frequencies, while Method (B) depends on the aperture size. We propose a method of re-introducing the missing piston and tip/tilt component to properly reconstruct the wavefronts. It still relies on Taylor’s Frozen Field Hypothesis, but only between adjacent wavefronts. We assume that the underlying structure does not change between the adjacent frames, but simply convects or shifts downstream. By minimizing the difference in the overlapping region, we can calculate the instantaneous convective speed and re-introduce piston and tip/tilt modes. In this manner the aperture-effect described in the Sec. B can be avoided. This stitching is repeated among adjacent frames to get a long streamwise strip of the wavefronts, as schematically shown in Figure [4]. Finally, trading space for time, we can compute the temporal evolution of the wavefront spectra and hopefully capture a better understanding of large-scale optical structures within a turbulent boundary layer.

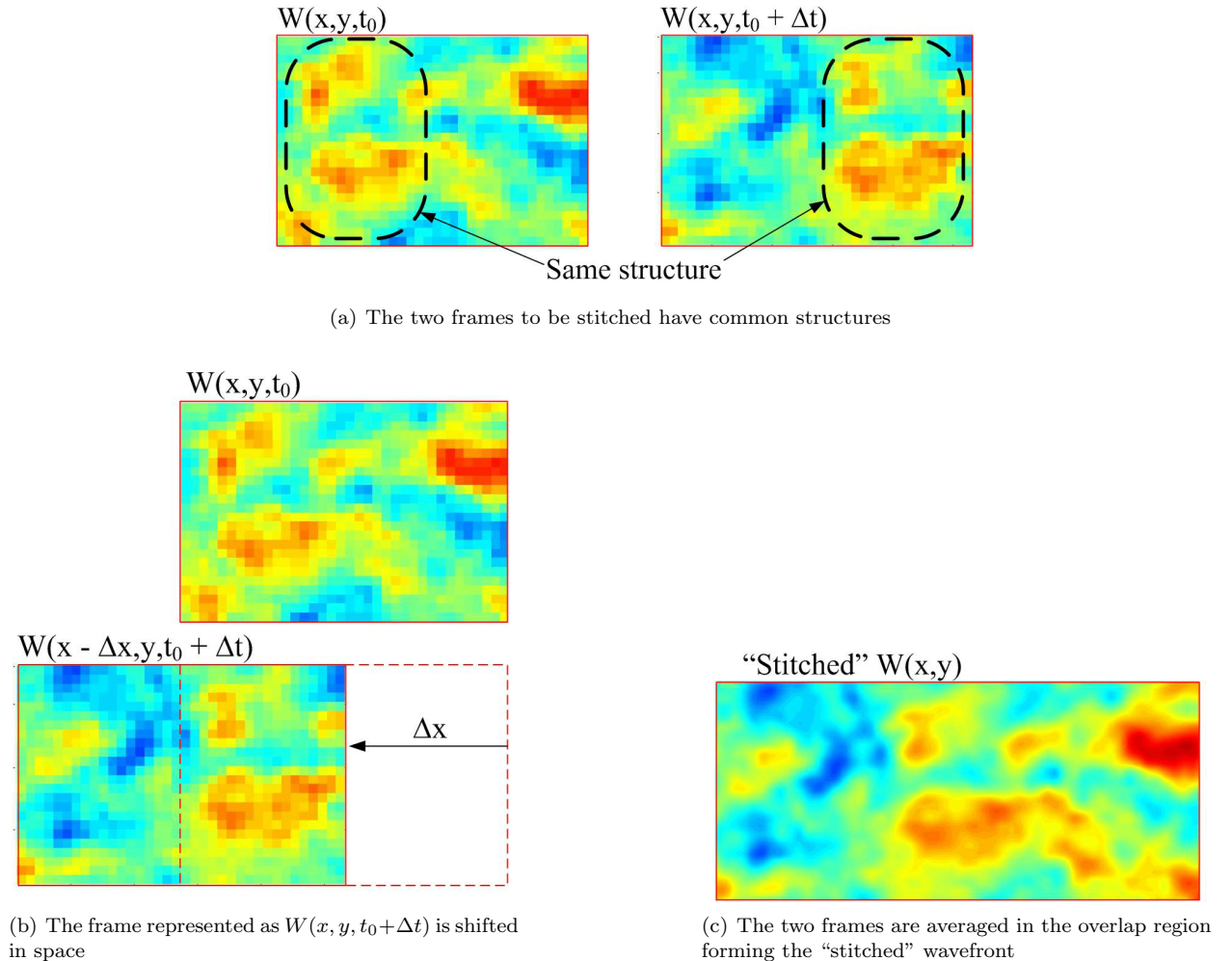


Figure 4. “Stitching” of two frames $W(x, y, t_0)$ and $W(x, y, t_0 + \Delta t)$. The flow direction is from left to right.

In order to properly combine the wavefront frames together, it is important to have some overlapping of the optical structure of sequential pairs of wavefronts. The amount of overlap is controlled by the frame rate of the high speed camera used as well as the instantaneous convective velocity of the aberrations.

If the distance the optical structures move between the subsequent frames is less than the aperture size, the distance the structure moves between frames can be found by cross-correlating wavefronts with different streamwise offsets. Finding the largest correlation will give the distance and dividing it by the time difference between frames will give the average convective velocity of the optical structures for a given subsequent pair of wavefronts.

The recombination used in this paper allows for deviations in instantaneous convective velocity from wavefront to wavefront. This is the reasoning behind the use of the term quasi-instantaneous frozen flow. The frame rate of the camera is a fixed experimental quantity so only the instantaneous convective velocity of the aberrations must be computed. In previous work, it was determined that the average convective velocity of the aberrations caused by an optically active boundary layer was about $0.82 - 0.85U_\infty$.¹⁷ In this work we sought to develop a method for accurately determining instantaneous convective velocity, rather than average velocity.

In order to determine the instantaneous convective velocity, averaged over the aperture, of the optical structures the wavefront mesh was first refined by using a cubic interpolation. Then, a 2D cross correlation was computed as illustrated in Eq. [2],

$$C[\Delta x] = \frac{1}{n} \sum_{x,y} \frac{(w_1(x,y) - \bar{w}_1)(\tilde{w}_2(\Delta x, y) - \bar{\tilde{w}}_2)}{\sigma_{w_1} \sigma_{\tilde{w}_2}} \quad (2)$$

where w_1 and w_2 are adjacent wavefronts. The tilde is used here to denote a tip, tilt, piston dithered wavefront. To properly stitch wavefronts, tip, tilt, and piston removal must be accounted for. As described in greater detail in Section 1, an iterative scheme is used as any tip, tilt, and piston added will naturally change the cross correlation. The process of correcting tip, tilt, and piston modes and then computing the cross correlation must be repeated until there is no appreciable change in cross correlation. Once convergence has been achieved, the offset from one frame to another could then be computed by determining the maximum of the resulting 2D cross correlation. This offset is by definition a whole number as the cross correlation is computed on discrete data. In reality the offset is not a whole number value. To compensate for this a parabola is fit through the maximum cross correlation value as well as its neighbors on either end. The maximum of the parabola is then used as the true spatial offset between the two frames.

After the offset is determined in index space the physical shift distance can be determined as the mesh spacing is a known quantity. The spacing between the lenslets in the wavefront sensor is known. The mesh spacing can then be given a physical quantity as the refined mesh covers the same physical space as the unrefined mesh. Using the frame rate of the camera and known physical shift distance the convective velocity of the wavefront can be determined. The process for determining the convective velocity of the wavefront can be broken down into 5 steps

1. Refine the wavefront mesh using a cubic interpolation.
2. Compute offset between two frames using the maximum of a 2D cross correlation with different stream-wise offsets.
3. Refine offset by fitting a parabola to the maximum correlation coefficient and its neighbors.
4. Using the known SHWFS lenslet spacing and the current number of mesh points to determine physical mesh spacing.
5. Using the frame rate of the camera and the physical mesh spacing determine the convective velocity of that wavefront.

By applying this procedure for many wavefronts continuously collected in time, a distribution of convective velocity can be extracted. An example of a histogram of the computed convective velocities, using wavefronts from ND experiments, can be seen in Figure [5]. The distribution is clearly skew left with a mean of $0.88U_\infty$. It is currently being investigated why convective speed measured in this manner produces a higher value than seen in previous experiments.¹⁷

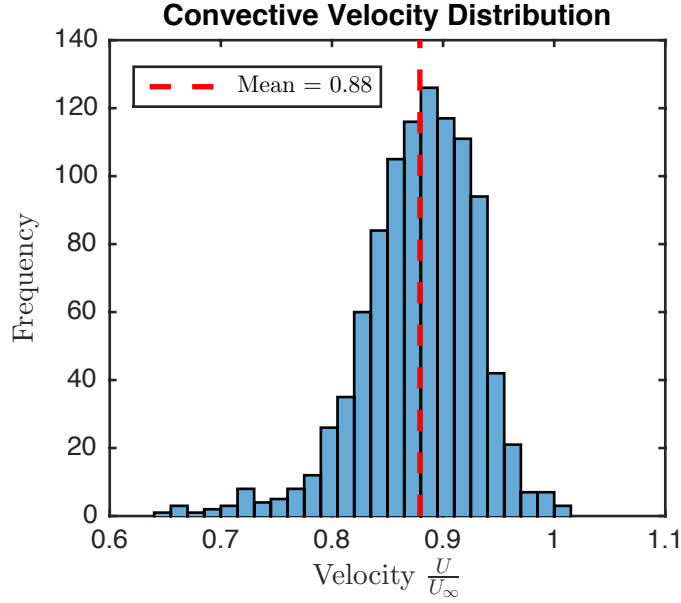


Figure 5. Convective velocity distribution of ND wavefront boundary layer data

1. “Stitching Algorithm” Description

The process for determining convective velocity and for stitching wavefront frames can be described in greater detail. The maximum of the cross correlation as seen in Eq. [2] is in reality a guess for the actual shift between wavefront frames. The tip, tilt, and piston must be matched in the overlapping region between frames. But, when the tip, tilt, and piston is modified in the overlapping regions between frames, the maximum of the cross correlation might change. Therefore we have an iterative algorithm where the computed shift between iterations is being driven to zero.

```

 $w_1 \leftarrow w_1;$ 
 $\tilde{w}_2 \leftarrow w_2;$ 
 $shift \leftarrow 0;$ 
while  $|shift - prevShift| \geq \epsilon$  do
   $shift \leftarrow \max(C[\Delta x]);$ 
   $\tilde{w}_2 \leftarrow \tilde{w}_2(x + shift, y);$ 
   $OR \leftarrow w_1 \cap \tilde{w}_2;$ 
   $A, B, C \leftarrow \min_{OR} \int (w_1 - \tilde{w}_2)^2 dOR;$ 
   $\tilde{w}_2 \leftarrow \tilde{w}_2 + Ax + By + C;$ 
   $prevShift \leftarrow shift;$ 
end

```

Algorithm 1: Stitching Algorithm

First, w_1 and \tilde{w}_2 are set to the two frames to be stitched. The computed shift is set to zero and the iterative scheme begins. The maximum cross correlation between the frames is computed and \tilde{w}_2 is shifted in x based upon that cross correlation. The tip (A), tilt (B), and piston (C) in the overlapping region between frames is computed by driving the RMS error between w_1 and \tilde{w}_2 to zero. Next, \tilde{w}_2 is updated based upon the aforementioned computed tip, tilt, and piston. The process is repeated until the computed shifts between iterations converges.

If added tip, tilt, and piston is small, then the iterative scheme can be avoided and the TTP corrected \tilde{w}_2 can be stitched to w_1 after just one iteration. This simplification was used in this work. Finally to combine the two frames together we multiplied the first frame by a weighting function in the overlapping region that linearly varied from one to zero. We then multiplied the second frame by a weighting function in the overlapping region that linearly varies from zero to one and summed the two frames. This ensured more accurate data collected toward the center of the wavefront was more heavily weighted.

The aforementioned computed velocities can then be used to compute the precise overlap between frames. Once the overlap region between frames is known tip, tilt, and piston between adjacent wavefronts can be adjusted such that neighboring frames have identical tip, tilt, and piston in the overlapping region. The neighboring frames can then be combined into one long strip. This process essentially trades time for space and reveals large scale boundary layer structures that were previously very difficult to discern.

This algorithm was repeated until all selected sequential wavefronts have been combined. There is certainly some evolution between neighboring frames, particularly in the higher frequency smaller scale structures. But, it has been shown in previous work that large scale structures are more optically active and therefore more pertinent when considering optical systems.¹⁷

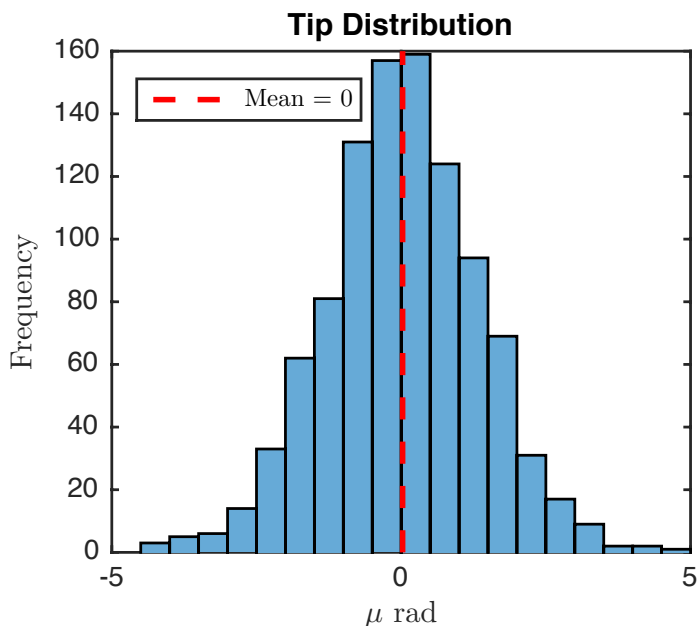


Figure 6. Histogram of tip distribution from ND data.

As mentioned before, the tip/tilt is easily corrupted during optical measurements and therefore hard to measure accurately. In the proposed combining algorithm the tip/tilt, needed to properly combine wavefronts, is restored and can be analyzed. An example of the probability distribution of the tip/tilt is presented in Figure [6]. It provides very useful requirements for properly designing Fast Steering Mirror (FSM) systems, commonly used in adaptive-optics systems,²⁰ to compensate for tip/tilt. FSMs are widely used in free-space communication systems and directed energy systems.

Figure [7] presents two examples of recombined wavefronts from the high-speed ND experiment shown alongside its corresponding instantaneous convective velocity. Each point on the convective velocity plot represents the center of a wavefront. One can clearly see large scale, on the order of 1-2 boundary-layer thicknesses, meandering structures present in the boundary layer. Similar meandering large-scale structures were observed in velocity fields.²¹ Without the technique outlined in this paper, evidence of these structures is much more difficult to see in individual small-aperture wavefronts.

Preliminary analysis has shown that there seems to be some correlation between the presence of the large structures and the velocity deficit (i.e the velocity smaller than the mean convective velocity). This is evident at the streamwise locations between 1 and 3.5 δ of Figure [7(a)] and between 2 and 3 δ of Figure [7(b)]. Currently, these correlations between large structures and velocity deficit are being studied more in depth.

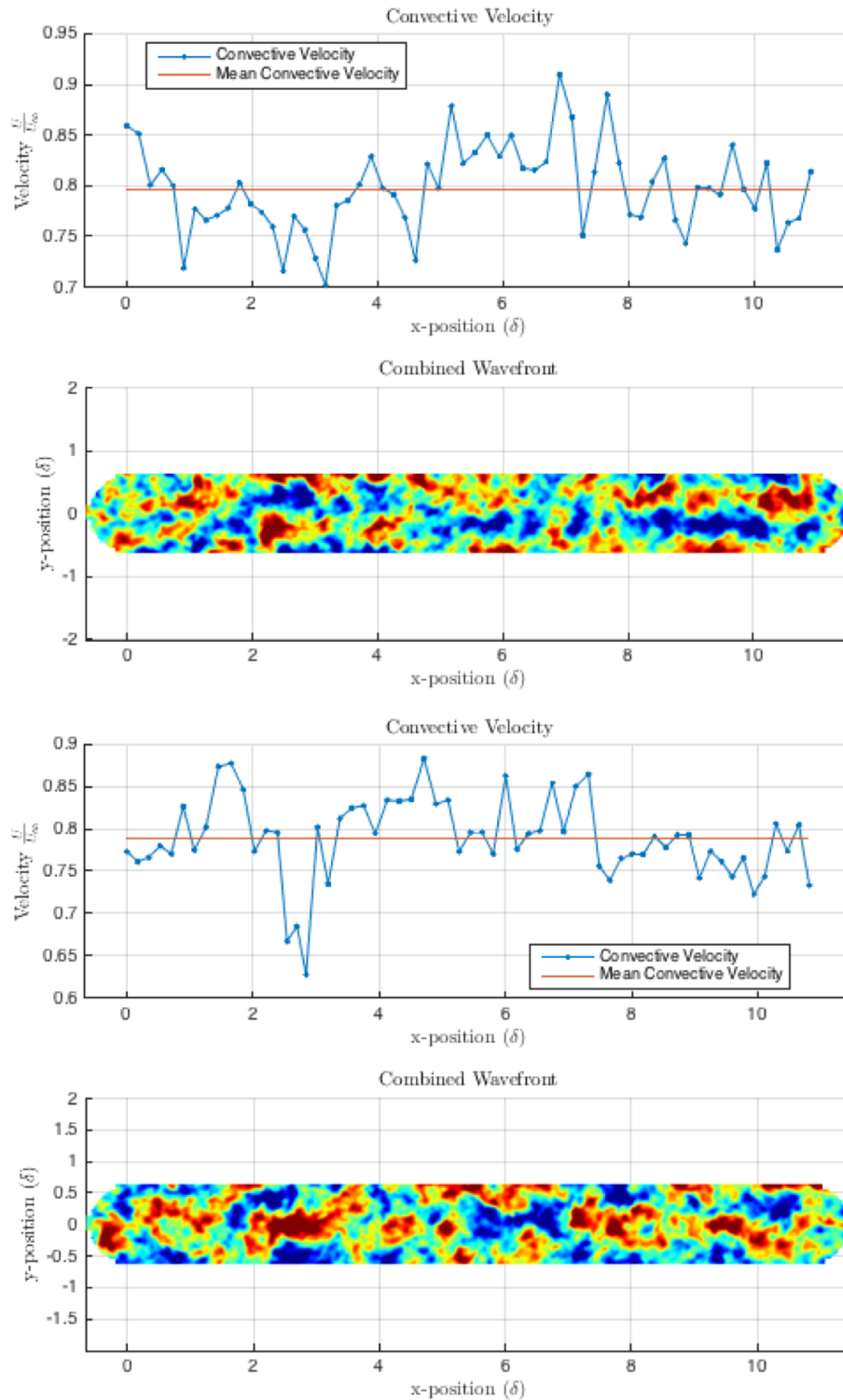


Figure 7. Examples of Combined wavefronts from the Caltech experiment plotted with corresponding instantaneous convective velocity.

Once wavefronts are restored over a large streamwise distance, wavefront energy spectra can be computed. The resulted premultiplied wavefront energy spectra from low- Re_θ Caltech experiment is presented in Figure [8]. Most of the optical energy corresponds to structures on the order of the boundary-layer thickness or larger.

The wavefront spectrum for high-speed Notre Dame experiment, also shown in Figure [8], reveals that

most of the optical energy shifts to a lower Strouhal number of $St_\delta \approx 0.2$, indicating that the dominant large-scale structure grows larger at higher Reynolds numbers. This observation is consistent with similar conclusions obtained from hot-wire data.²² Hutchins and Marusic found a distinct shift in peak location from $\lambda/\delta = 1.6$ for the low $Re_\tau = 1000$ case to $\lambda/\delta \approx 6$ for the high $Re_\tau = 7300$ case. Converting Strouhal number to λ/δ using Eq. [4] we found for our low $Re_\tau = 1200$ case $\lambda/\delta \approx 2.2$ and for our high $Re_\tau = 4780$ case $\lambda/\delta \approx 4.1$. These findings are consistent with Hutchins and Marusic.²²

$$St_\delta = \frac{f \cdot \delta}{U_\infty} = \frac{f U_c \cdot \delta}{U_c U_\infty} = \frac{1 U_c \cdot \delta}{\lambda U_\infty} = \frac{\delta U_c}{\lambda U_\infty} \quad (3)$$

$$\implies \frac{\lambda}{\delta} = \frac{U_c}{U_\infty} \frac{1}{St_\delta} \quad (4)$$

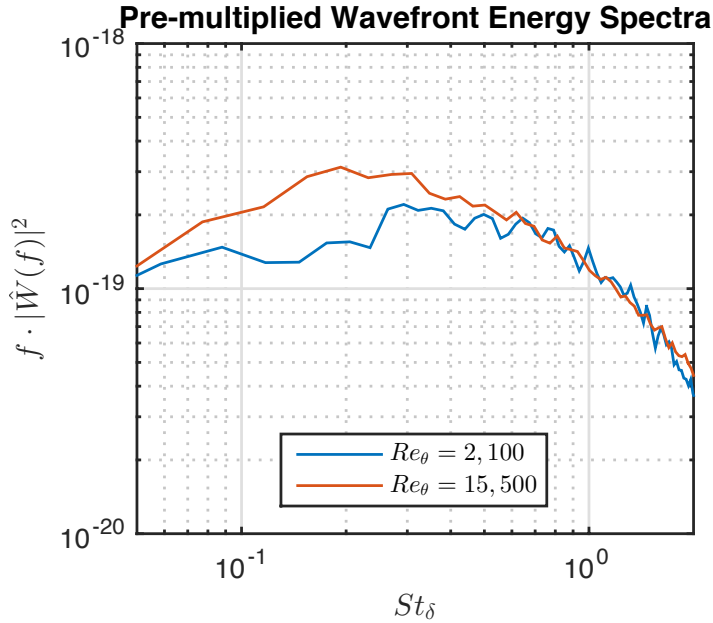


Figure 8. Premultiplied wavefront energy spectra, computed from combined wavefronts and directly from the deflection angle spectrum.

Finally 2D autocorrelations of wavefronts were computed using Eq. [5]. The same process of time series construction as seen in Sec. [B] was used to generate varying aperture sizes for comparison. The centerline correlations can be seen in Figure [9].

$$C[\Delta x, \Delta y] = \overline{w(x, y)w(x + \Delta x, y + \Delta y)} \quad (5)$$

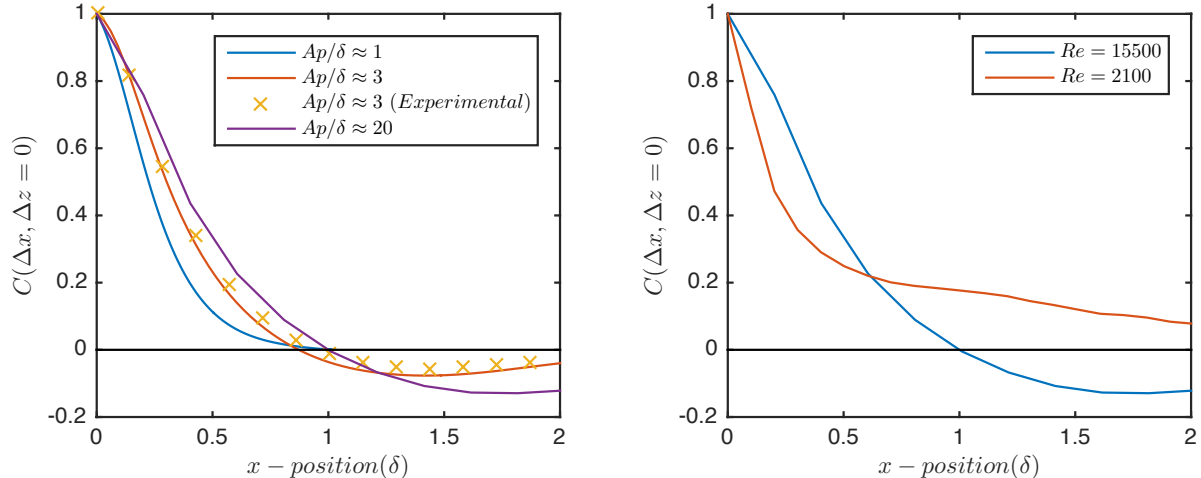


Figure 9. Streamwise center-line slice of 2D wavefront autocorrelation.

There is a distinct convergence in the correlation for $Ap/\delta > 3$. This verifies previous results stating that an aperture of about $Ap/\delta \approx 3 - 5$ is sufficient to capture large scale structures. In addition, the shape of the curves seen in Figure [9(a)] can provide information about the size of structures seen within the boundary layer. The slope of curve near zero or the location of the first zero crossing can provide estimates for structure size. Once again comparing results from the low Reynold’s number Caltech Experiment with the high Reynold’s number ND experiment the correlation coefficients of the Caltech experiment approach zero much faster. This points to a overall decrease in structure size as expected.²²

IV. Conclusion

Large scale boundary layer structures carry an important role in boundary-layer dynamics and as such they are of particular interest to researchers. In the past they have been primarily studied using hotwire and PIV techniques. In this work, measurements of aero-optical distortions due to turbulent boundary layers are presented and discussed. Aero-optical distortions are related to the density structure of the flow and carry important information about the large-scale structure. Wavefront sensing techniques are advantageous because they are non-intrusive by nature and can be conducted at very high speeds and Reynolds numbers. Measurements were conducted at low subsonic speed in Caltech’s Merrill Wind Tunnel facility at $M = 0.03$, as well as at transonic speed of $M = 0.4$ at Notre Dame’s Tri-Sonic facility. Optical wavefronts were collected over a range of sampling frequencies and spatial resolutions. Different techniques of calculating wavefront spectra were considered and compared and their various issues/limitations were discussed. Using a quasi-instantaneous frozen flow technique we were able to eliminate most of these issues inherent in wavefront collection. Trading time for space we were able to generate “stitched” wavefronts representative of a large convectively-frozen boundary layer structure. By cross-correlating the adjacent wavefronts, “instantaneous” convective speeds were also extracted and analyzed; they were shown to depend on the strength of the underlying large-scale structure. Using this new technique and comparing the wavefront spectra data at two different Reynold’s number we were able to observe the shift in energy to lower frequencies with increase in Reynold’s number, in agreement with similar trends reported by other researchers using traditional hotwire techniques. In this manner we demonstrated that large-scale boundary layer structures can be analyzed using optical wavefront techniques. In the future we will extend this work to larger apertures to account for the streamwise spatial evolution of the boundary layers, and to supersonic and hypersonic speeds.

Acknowledgments

The authors would like to acknowledge Adam Smith, Theresa Saxton-Fox, and Beverly McKeon to their help in collecting wavefront data in the Merrill wind tunnel at Caltech.

References

- ¹Marusic, I., McKeon, B. J., Monkewitz, P. A., Nagib, H. M., Smits, A. J., and Sreenivasan, K. R., “Wall-bounded turbulent flows at high Reynolds numbers: Recent advances and key issues,” *Physics of Fluids*, Vol. 22, No. 6, 2010.
- ²Smits, A. J., McKeon, B. J., and Marusic, I., “High-Reynolds Number Wall Turbulence,” *Annual Review of Fluid Mechanics*, Vol. 43, 2011, pp. 353–375, <http://dx.doi.org/10.1146/annurev-fluid-122109-160753>.
- ³Dennis, D. J. C. and Nickels, T. B., “Experimental measurement of large-scale three-dimensional structures in a turbulent boundary layer. Part 1. Vortex packets,” *Journal of Fluid Mechanics*, Vol. 673, 2011, pp. 180–217.
- ⁴Guala, M., Hommema, S. E., and Adrian, R. J., “Large-scale and very-large-scale motions in turbulent pipe flow,” *Journal of Fluid Mechanics*, Vol. 554, 2006, pp. 521–542.
- ⁵Zhou, J., Adrian, R. J., Balachandar, S., and Kendall, T. M., “Mechanisms for generating coherent packets of hairpin vortices in channel flow,” *Journal of Fluid Mechanics*, Vol. 387, 1999, pp. 353–396.
- ⁶Adrian, R. J., Meinhardt, C. D., and Tomkins, C. D., “Vortex organization in the outer region of the turbulent boundary layer,” *Journal of Fluid Mechanics*, Vol. 422, 2000, pp. 1–54.
- ⁷Jumper, E. J. and Fitzgerald, E. J., “Recent advances in aero-optics,” *Progress in Aerospace Sciences*, Vol. 37, No. 3, 4 2001, pp. 299–339.
- ⁸Wang, M., Mani, A., and Gordeyev, S., “Physics and Computation of Aero-Optics,” *Annual Review of Fluid Mechanics*, Vol. 44, No. 1, 2012, pp. 299–321, <http://dx.doi.org/10.1146/annurev-fluid-120710-101152>.
- ⁹Gordeyev, S., Jumper, E., and Hayden, T., “Aero-Optics of Supersonic Boundary Layers,” Aerospace Sciences Meetings, American Institute of Aeronautics and Astronautics, 01/04; 2016/01 2011, 05; M1: 0; doi:10.2514/6.2011-1325.
- ¹⁰Gordeyev, S., Rennie, M. R., Cain, A. B., and Hayden, T., “Aero-Optical Measurements of High-Mach Supersonic Boundary Layers,” AIAA Aviation, American Institute of Aeronautics and Astronautics, 06/18; 2016/01 2015, 05; M1: 0; doi:10.2514/6.2015-3246.
- ¹¹Gordeyev, S. and Juliano, T. J., “Optical Characterization of Nozzle-Wall Mach-6 Boundary Layers,” AIAA SciTech, American Institute of Aeronautics and Astronautics, 01/02; 2016/01 2016, 05; M1: 0; doi:10.2514/6.2016-1586.
- ¹²Dennis, D. J. C. and Nickels, T. B., “On the limitations of Taylor’s hypothesis in constructing long structures in a turbulent boundary layer,” *Journal of Fluid Mechanics*, Vol. 614, 2008, pp. 197–206.
- ¹³Gordeyev, S., Smith, A. E., Saxton-Fox, T., and McKeon, B. J., “Studies of the large-scale structure in adiabatic and moderately-wall-heated subsonic boundary layers,” 2015.
- ¹⁴Cress, J. A., “Optical Aberrations Caused by Coherent Structures in a Subsonic, Compressible, Turbulent Boundary Layer,” 2010.
- ¹⁵Gordeyev, S., Cress, J. A., Smith, A., and Jumper, E. J., “Aero-optical measurements in a subsonic, turbulent boundary layer with non-adiabatic walls,” *Physics of Fluids*, Vol. 27, No. 4, 2015.
- ¹⁶Southwell, W. H., “Wave-front estimation from wave-front slope measurements,” *J.Opt.Soc.Am.*, Vol. 70, No. 8, Aug 1980, pp. 998–1006.
- ¹⁷Gordeyev, S., Smith, A. E., Cress, J. A., and Jumper, E. J., “Experimental studies of aero-optical properties of subsonic turbulent boundary layers,” *Journal of Fluid Mechanics*, Vol. 740, 2014, pp. 214–253.
- ¹⁸Siegenthaler, J. and Jumper, E., “Guidelines for adaptive-optic correction based on aperture filtration,” 2009, ID: TN_proquest304974444.
- ¹⁹Lucca, N. D., Gordeyev, S., and Jumper, E., “The Study of Aero-Optical and Mechanical Jitter for Flat Window Turrets,” Aerospace Sciences Meetings, American Institute of Aeronautics and Astronautics, 01/09; 2016/01 2012, 05; M1: 0; doi:10.2514/6.2012-623.
- ²⁰Wang, K. and Wang, M., “Aero-optics of subsonic turbulent boundary layers,” *Journal of Fluid Mechanics*, Vol. 696, 2012, pp. 122–151.
- ²¹Hutchins, N. and Marusic, I., “Evidence of very long meandering features in the logarithmic region of turbulent boundary layers,” *Journal of Fluid Mechanics*, Vol. 579, 2007, pp. 1–28.
- ²²Hutchins, N. and Marusic, I., “Large-Scale Influences in Near-Wall Turbulence,” *Philosophical Transactions: Mathematical, Physical and Engineering Sciences*, Vol. 365, No. 1852, 2007, pp. 647–664.